GPS Solutions (2026) 30:11
https://doi.org/10.1007/s10291-025-01979-6

RESEARCH

Precise point positioning with an adaptive geometry-free cycle slip detection threshold under complex ionospheric conditions

Long Tang[1] · Luheng Zhou[1] · Fan Xu[1] · Jiahuan Hu[2] · Xiaohong Zhang[3]

Received: 6 June 2025 / Accepted: 3 October 2025 / Published online: 23 October 2025
© The Author(s) 2025

Abstract
Global navigation satellite system (GNSS) precise point positioning (PPP) performance experiences significant degradation under complex ionospheric conditions, particularly during geomagnetic storm events. To address this challenge, this study develops an adaptive geometry-free (GF) cycle slip detection threshold model, leveraging GNSS Doppler measurements to reduce the incorrect cycle slip detection, thereby enhancing the accuracy and reliability of GNSS PPP. The proposed threshold model is fitted using Doppler index data extracted from 110 International GNSS Service (IGS) stations on the 11th May 2024 when an extreme geomagnetic storm occurred. 72 IGS stations which are not used in modeling on the same day are employed to validate its performance. The results show that PPP with adaptive GF cycle slip detection threshold can achieve positioning accuracy improvements by 42.4% and 37.2% in horizontal and vertical directions, respectively, compared with traditional strategy. Furthermore, positioning accuracy improvements of 63.1% and 50.1% in horizontal and vertical are obtained with data from another geomagnetic storm event on the 11th October 2024, which further demonstrates the efficiency and uniformity of proposed model. Comparison of positioning accuracy with tight and loose thresholds during the ionospheric quiescence periods also verifies the adaptability of the built model.

Keywords Global navigation satellite system (GNSS) · Precise point positioning (PPP) · Doppler index (DI) · Cycle slip detection · Ionosphere activity

Introduction

Precise point positioning (PPP) is an advanced Global Navigation Satellite System (GNSS) positioning technique that enables high-precision location-based-services using a single receiver (Zumberge et al. 1997; Kouba and Héroux 2001). Due to its advantages, PPP technique has been widely applied in geodesy and geophysics (Zhang and Andersen 2006; Li et al. 2013), ionospheric monitoring (Zhang et al. 2012; Liu et al. 2019), meteorology (Shi et al. 2014), and other areas relevant to spatial information in the recent two decades. However, the practical applications of PPP still face many challenges, which include, e.g., PPP service degradation or interruption because of ionospheric activities (Chen et al. 2008; Marques et al. 2018; Yang et al. 2020).

Under complex ionospheric conditions, ionospheric total electron content (TEC) varies sharply, which significantly affects the raw GNSS measurements, thereby degrading the positioning performance of GNSS PPP. Moreno et al. (2011) indicated the positioning errors can be up to several meters for a single-epoch PPP during the periods when large TEC variation occurred in low latitudes. With statistical analysis of PPP results in years 2001, 2004, and 2011, Rodríguez-Bilbao et al. (2015) further confirmed that high TEC variations leaded to increased positioning errors. As one of the most representative complex ionospheric events, the geomagnetic storm exerts a notably adverse influence on the PPP results. Luo et al. (2018) investigated the PPP performance using global international GNSS service (IGS) stations during various geomagnetic storm periods. Their statistical results showed that the number of IGS stations

✉ Jiahuan Hu
jiahuanhu95@163.com

[1] School of Civil and Transportation Engineering, Guangdong University of Technology, Guangzhou, China

[2] Department of Land Surveying and Geo-Informatics, The Hong Kong Polytechnic University, Hong Kong, China

[3] Chinese Antarctic Center of Surveying and Mapping, Wuhan University, Wuhan 430079, China

with positioning error root mean square (RMS) larger than 0.5 m increased with the magnitude increment of geomagnetic storm. Lu et al. (2020) assessed PPP performance during St. Patrick's Day geomagnetic storm in 2015 in Hong Kong, and indicated that the PPP accuracy was vastly decreased with a maximum daily 3D positioning error of 1.3 m. Similarly, Zakharenkova and Cherniak (2021) indicated the 3D error of PPP for GNSS stations in American area had risen to several meters during the geomagnetic storm on 7–8th September 2017. Recently, Danilchuk et al. (2025) reported the impact of May 2024 extreme geomagnetic storm on GNSS positioning. Their results indicated the PPP positioning errors increased 1.5–5 times at the boundary of the auroral oval, moreover, increased positioning errors propagated according to the shift of the auroral oval boundary.

Many scholars have realized that the key reason for degraded positioning performance under complex ionospheric conditions is frequent cycle slip misjudgments(Zhang et al. 2014). Therefore, correctly detecting cycle slips is beneficial to improve the PPP positioning performance under such ionospheric activities. However, during active ionospheric environments, cycle slips are wrongly detected using the classical geometry-free (GF) phase combination (Li et al. 2022). To avoid this issue, Zhang et al. (2014) suggested to set an empirical loose threshold for the GF combination method, furthermore, Rodríguez-Bilbao et al. (2015) recommended directly disabling the GF combination method. But an overly loose threshold or disabling GF combination method will lead to the miss-detection of potential small cycle slips. Luo et al. (2022) established a GF cycle slip detection threshold model based on the rate of TEC index (ROTI). This model can set an adaptive GF cycle slip detection threshold according to the ROTI value. Their results showed the adaptive threshold model can improve the PPP positioning accuracy by 14.0% and 23.1% in the horizontal and vertical directions for global stations during the geomagnetic storm on 8th September 2017 compared to conventional strategy. However, the ROTI value is computed based on carrier-wave phase measurements, which means that cycle slip detection needs to be conducted before obtaining the ROTI value, thus limiting the application of their GF cycle slip detection threshold model.

Indeed, there is another commonly used GNSS observation type, the Doppler measurement, which has the advantage of free from phase cycle slips (Banville and Langley 2012). Luo et al. (2023) employed the dual-frequency Doppler measurements to extract the TEC variation and defined a ROTI-like index termed the Doppler index (DI), which exhibited an average correlation coefficient of 0.95 with ROTI. Given its strong correlation with ROTI, it is reasonable to predict that the DI can also be employed for modeling the adaptive GF cycle slip detection threshold.

In this study, the DI is utilized to establish the adaptive GF cycle slip detection threshold model. The rest of the sections is organized as follows. Firstly, the methods and data for DI calculation and threshold modelling are described. Subsequently, the feasibility of the threshold model on PPP is investigated and validated using global GNSS stations. Finally, conclusions are drawn based on the positioning experiment.

Data and method

This section begins with a brief introduction and illustration of the effect of cycle slips on ROTI computation, motivating the development of the proposed method in using DI values for building a model. Then, an introduction of a truly occurred extreme geomagnetic storm event is given, followed by the dataset description used in this study. Moreover, the detailed method is introduced to establish an adaptive GF cycle slip detection threshold model.

Effect of cycle slips on ROTI computation

Simulated cycle slips of 1-cycle are added to L1 phase measurements of satellite G09 at station AREG for every hour from 1:00–7:00 UT on 11th October 2024. Threshold of 0.5 m for GF method, which are commonly used for TEC calculation, is set for cycle slip detection. Figure 1 shows the time series of the calculated ROTIs. The blue line represents the ROTI time series of the original data, and the red line represents the ROTI time series after adding the simulated cycle slips. It is obvious that none of the simulated 1-cycle cycle slips is detected during the ionospheric disturbances, and each simulated cycle slip has an adverse effect on the ROTI computation. Therefore, if directly using ROTIs to build the adaptive GF threshold model, the abnormal ROTI values would impact the built model and further affect the model performance in PPP.

Geomagnetic storm event and GNSS doppler data

An extreme geomagnetic storm event occurred on 11 May 2024. Disturbance storm time index (Dst), interplanetary magnetic field of the z-component (IMF-Bz) and planetary K index (Kp) are the three commonly used indices in indicating ionospheric activities. Figure 2 shows the time series of Dst, IMF-Bz and Kp indices from 10th May 2024 to 12th May 2024. The Dst index rose to 66 nT at about 17:00 UT on 10 May 2024, then declined rapidly at around 18:00 UT on 10th May 2024, similarly, the IMF-Bz index also began

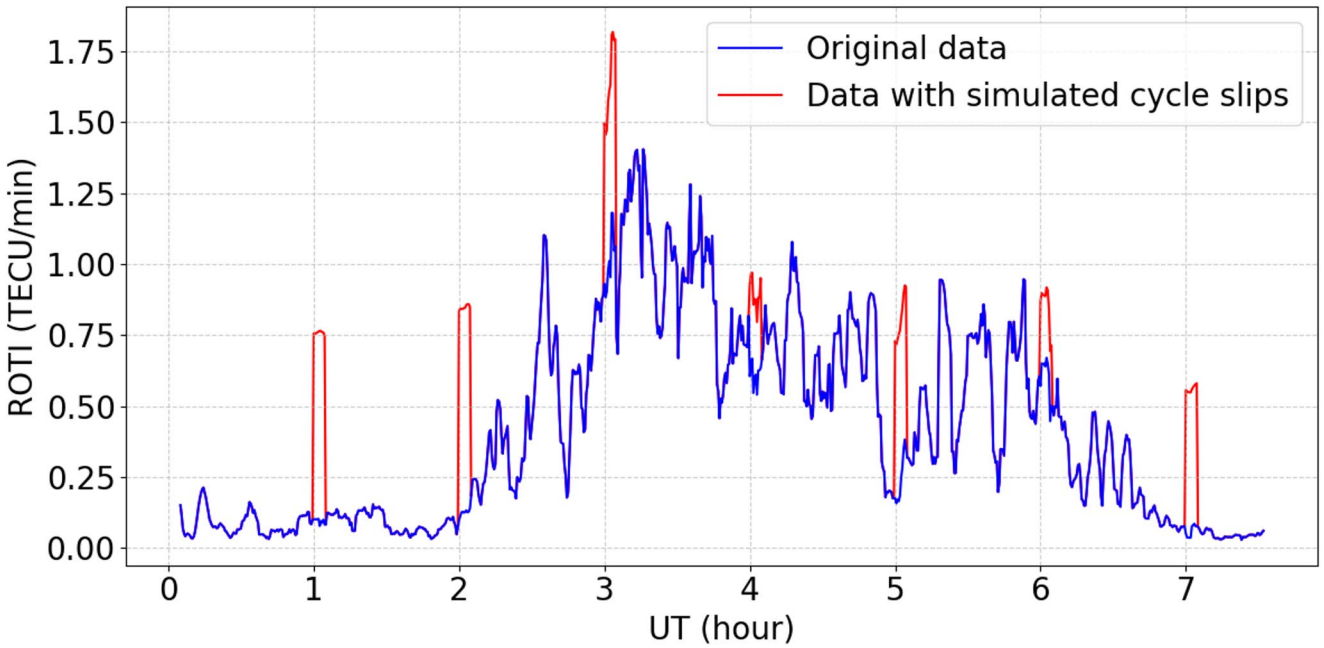


Fig. 1 ROTIs calculated with original data (blue line) and the same with simulated cycle slips (red line) for satellite G09 at GNSS station AREG on 11th October 2024

to fluctuate significantly at this time. Moreover, it can also be noticed that the Kp index began to rise after 13:00 UT on 10th May 2024, and rose rapidly to 9+level. The Dst index dropped to the lowest of -406 nT at around 2:00 UT on 11th May 2024. Therefore, in this study, model construction and positioning validation are conducted based on this event.

There is a total of 182 IGS stations supporting dual-frequency Doppler observations on 11th May 2024, as shown in Fig. 3. Among them, 110 stations (blue dots) are randomly selected for geometry-free (GF) cycle slip threshold modeling, and other 72 stations (red dots) are used to verify the PPP performance using the built model on the same day.

Adaptive geometry-free cycle slip detection threshold model

The dual-frequency geometry-free (GF) phase combination Φ_{GF} is:

$$\Phi_{GF} = \Phi_1 - \Phi_2 = (\lambda_1 N_1 - \lambda_2 N_2) - I_{\mathrm{GF}} + \epsilon \tag{1}$$

where $\Phi_1$and Φ_2 are the phase measurements in unit of meter at frequencies f_1 and f_2, respectively. λ_1 and λ_2 are the phase wavelengths on corresponding frequencies, N_1 and N_2 are the phase ambiguities. $I_{\mathrm{GF}} = I_1 - I_2 = 40.3 \cdot TEC \cdot \left(1/f_1^2 - 1/f_2^2\right)$ is the ionospheric delay term, and ϵ is the GF combined phase noise. By calculating the differences of Φ_{GF} between successive epochs, the ambiguity term in Eq. (1) is eliminated if no cycle slip detected. Therefore, the magnitude of between-epoch differenced Φ_{GF}, i.e., $\Delta\Phi_{GF}$, depends on the time-differenced residual ionospheric delay ΔI_{GF}, where Δ is the time-differencing operator.

Generally, the value of ΔI_{GF} is very small with small time intervals, e.g., 1–30 s. Therefore, a tight empirical threshold of 0.05 m is usually set to detect cycle slips using GF combination, and the performance is good during ionosphere calm period. However, studies have shown that the empirical threshold cannot effectively deal with ionospheric anomalies, resulting in massive unnecessary ambiguity initialization because of false detected cycle slips, thus decreasing the positioning accuracy. Therefore, it is necessary to construct a GF cycle slip detection model that adaptively sets a threshold according to ionospheric changes.

The GNSS Doppler index (DI) is employed to fit the threshold model, and the definition of DI is as follows (Luo et al. 2023; Zhang et al. 2025):

$$D_i\lambda_i = \dot{\rho} + c\left(\dot{dt}_r - \dot{dt}^s\right) - \dot{I}_i + \dot{T} + \epsilon_i \tag{2}$$

$$\Delta D = D_1\lambda_1 - D_2\lambda_2 = \dot{I}_2 - \dot{I}_1 \tag{3}$$

$$DI = \frac{1}{40.3}\frac{f_1^2 f_2^2}{f_1^2 - f_2^2}\sqrt{?\Delta D^2? - ?\Delta D?^2} \tag{4}$$

where i is the frequency number and D_i is the Doppler measurement. $\dot{\rho}$ represents the geometric range rate between the satellite and receiver, c is the speed of light, $\dot{dt}^s$ and $\dot{dt}_r$ are the satellite and receiver clock bias rate, respectively. $\dot{I}_i$ is

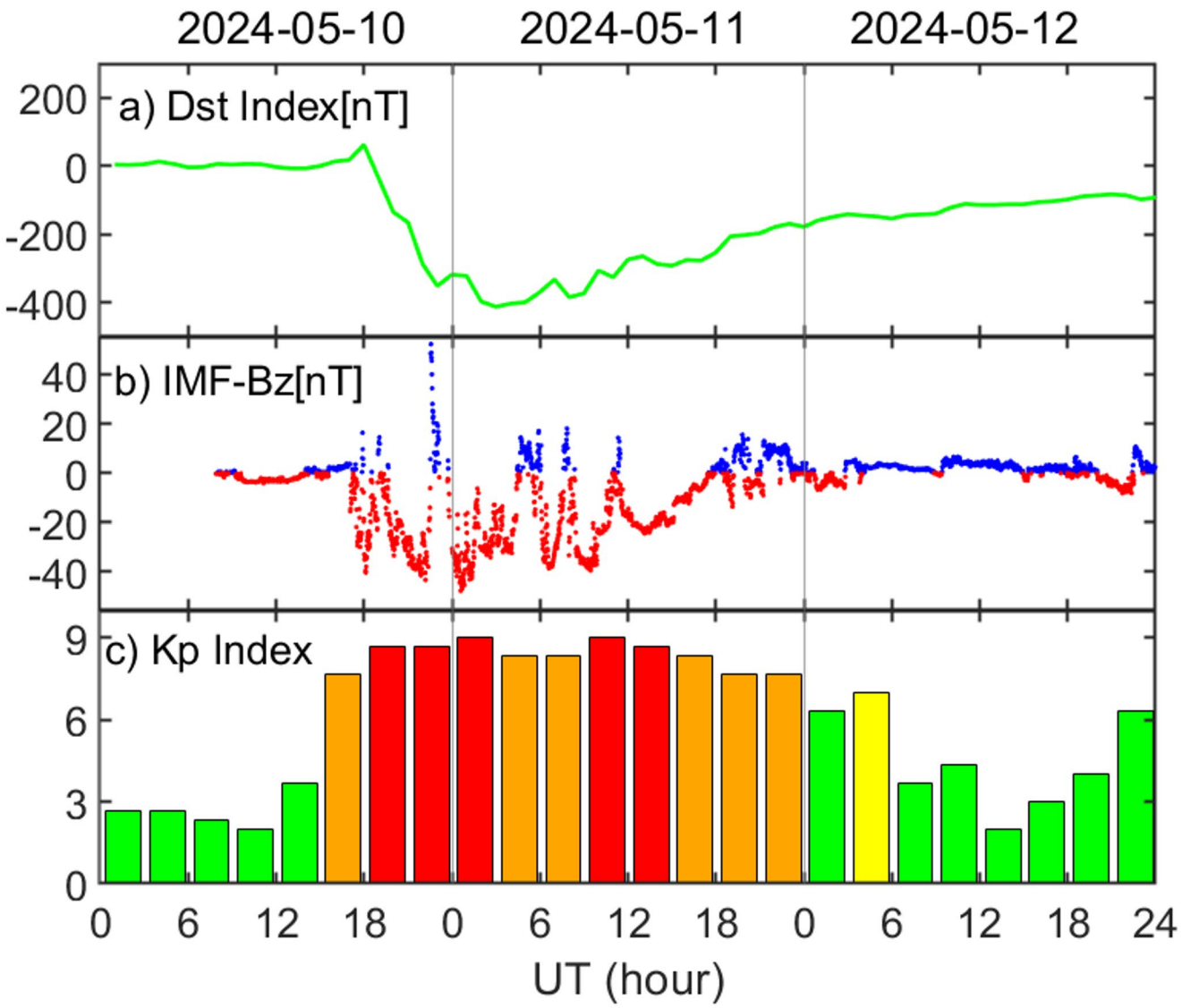


Fig. 2 Dst, IMF-Bz (The blue dots indicate greater than 0, and the red dots indicate less than 0) and Kp (The order of magnitude is indicated from green to red) indices from 10th May 2024 to 12th May 2024

the ionospheric delay rate, and $\dot{T}$ is the tropospheric delay rate. ϵ_i is the noise, and $?\cdot?$ represents the average operation. The unit of DI is TECU/min, which is consistent to the ROTI. In this study, same as the ROTI, a 5-minute sliding window is adopted to calculate the DI.

Figure 4 shows the correlation between $\Delta\Phi_{GF}$ and DI obtained from the GNSS data of 110 IGS stations on 11th May 2024. It can be seen that the distribution of $\Delta\Phi_{GF}$ is relatively concentrated when DI is between 0 and 1 $\mathrm{TECU/min}$. For $1 < \mathrm{DI} \leq 7\mathrm{TECU/min}$, $\Delta\Phi_{GF}$ increases along with the increase of DI, and the trend stops when $\mathrm{DI} = 7\mathrm{TECU/min}$. Therefore, a piecewise function is established with 1 and 7 as the demarcation points.

The value of 99.97th percentile of $\Delta\Phi_{GF}$ is taken as the constant threshold when DI is smaller than $1\mathrm{TECU/min}$. Similarly, the 99.97th percentile (3σ) values of $\Delta\Phi_{GF}$ are calculated with steps of 0.05 TECU/min for DIs in range of 1–7 $\mathrm{TECU/min}$, and a quadratic polynomial function is then fitted using the calculated 3σ values. For DI larger than 7 $\mathrm{TECU/min}$, a constant threshold is assigned. Finally, the adaptive GF cycle slip detection threshold model is built and expressed as:

$$|Th_{GF}(DI)| = \begin{cases} 0.180, & DI \leq 1 \\ -0.002DI^2 + 0.083DI + 0.099, & 1 < DI \leq 7 \\ 0.582, & DI > 7 \end{cases} \quad (5)$$

where Th_{GF} is the threshold of GF combination method in unit of meter.

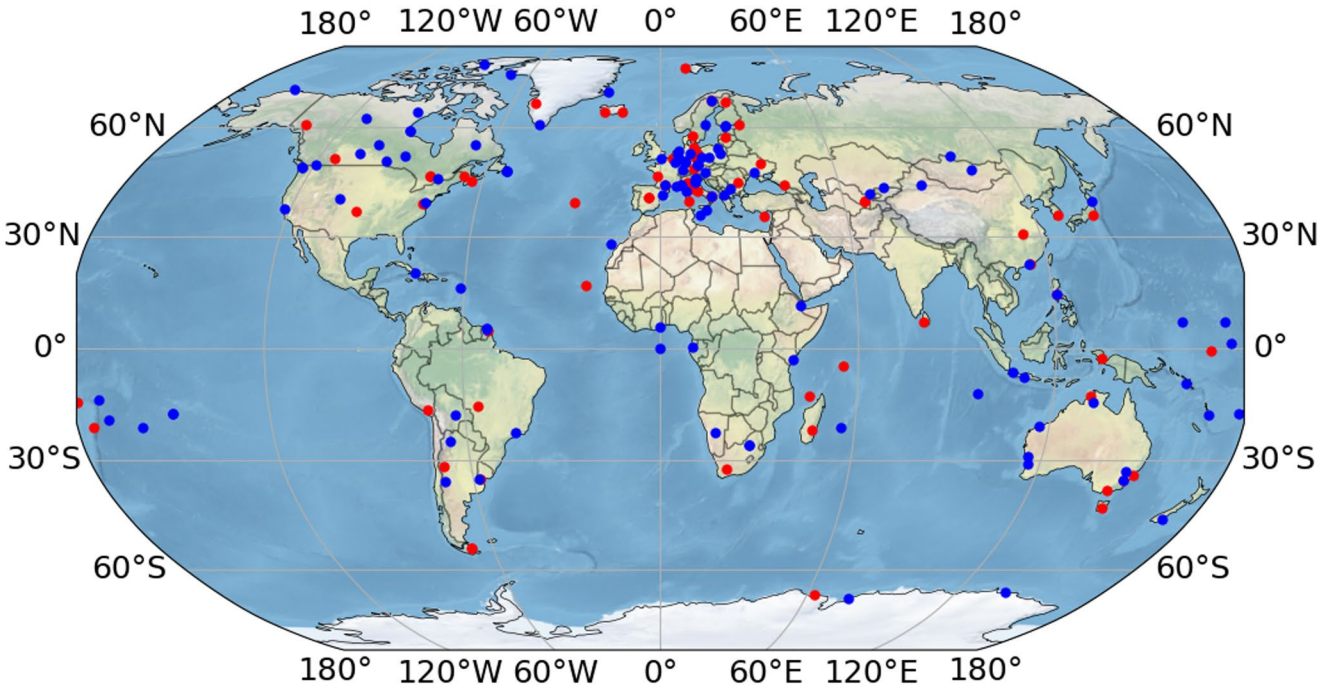


Fig. 3 The geographical distribution of IGS stations used in the experiment on 11th May 2024. The blue dots represent the stations used for modeling, while the red dots represent the stations used for PPP verification

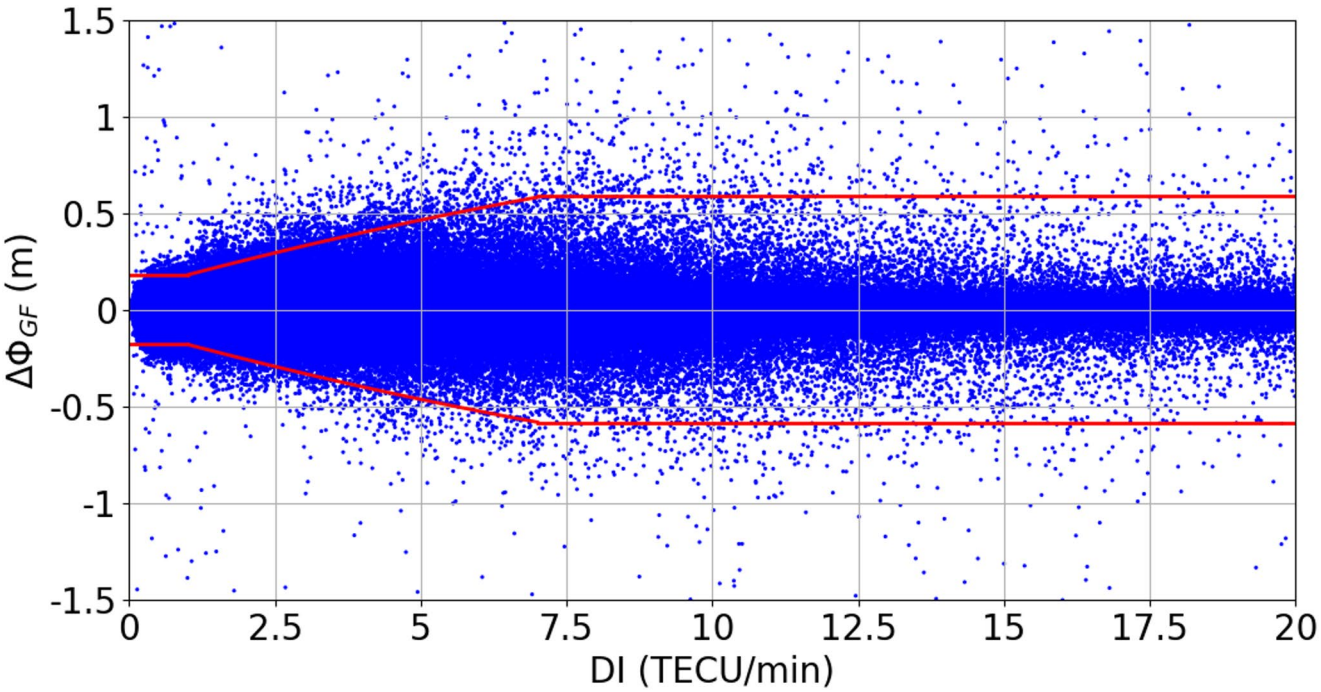


Fig. 4 Correlation between $\Delta\Phi_{GF}$ and DI using GNSS data from 110 IGS tracking stations. The blue dots represent DI and the corresponding $\Delta\Phi_{GF}$, the red lines represent the adaptive GF cycle slip detection threshold model

Table 1 Strategies of precise point positioning

Item	Strategies
Observations	Pseudorange and carrier phase observations on L1 and L2
System	GPS
Sampling interval	30 s
Elevation mask angle	15°
Precise satellite orbit	IGS precise products
Precise satellite clock	IGS precise products
Ionospheric delay	Ionospheric-free combination
Tropospheric delay	Est ZTD + Grad
Phase center offset	igs14.atx
Cycle slip detection strategy	TurboEdit method
Quality control strategy	Outlier detection and de-weighting based on posterior residuals

Experiments and results

This section performs kinematic PPP processing using 72 validation stations which are not used in model fitting on 11th May 2024 to assess the performance of the proposed model. In addition, the kinematic PPP results of 215 IGS tracking stations during another geomagnetic storm on 11th October 2024 were also analyzed and assessed to verify the universality of the proposed model. Table 1 summarizes the detailed processing strategies of PPP. Moreover, two schemes are designed for comparison, with Scheme 1 using the traditional fixed GF threshold of 0.05 m, and Scheme 2 with the adaptive GF threshold model proposed in this paper. The precise satellite orbit and precise satellite clock products are available from IGS and open-sourced software RTKLIB is adopted to process the experimental data.

Kinematic PPP results on 11th May 2024

Kinematic PPP positioning error time series of 3 IGS stations located in different latitude zones are first illustrated for analyzing, including FRDN (45.93° N, 66.66° W), PRDS (50.87° N, 114.29° W) and HOFN (64.27° N, 15.20° W). Secondly, the positioning accuracy of 72 stations is calculated to verify the performance of the model. Figure 5 shows the time series of GPS kinematic PPP solutions and the corresponding DIs of the 3 stations in the East, North and Up directions, respectively.

In Fig. 5, the blue lines represent the results of Scheme 1 and the red lines are the results of Scheme 2. The positioning error RMSs of the two schemes are labelled on the top right of the subplots as well. It is notable that the positioning accuracy of Scheme 2 is significantly improved compared with Scheme 1. For these 3 stations in different latitudes, the time series of positioning errors for the three directions are smoother with Scheme 2, with less outliers and spikes. The reason is that the adaptive GF threshold model of Scheme

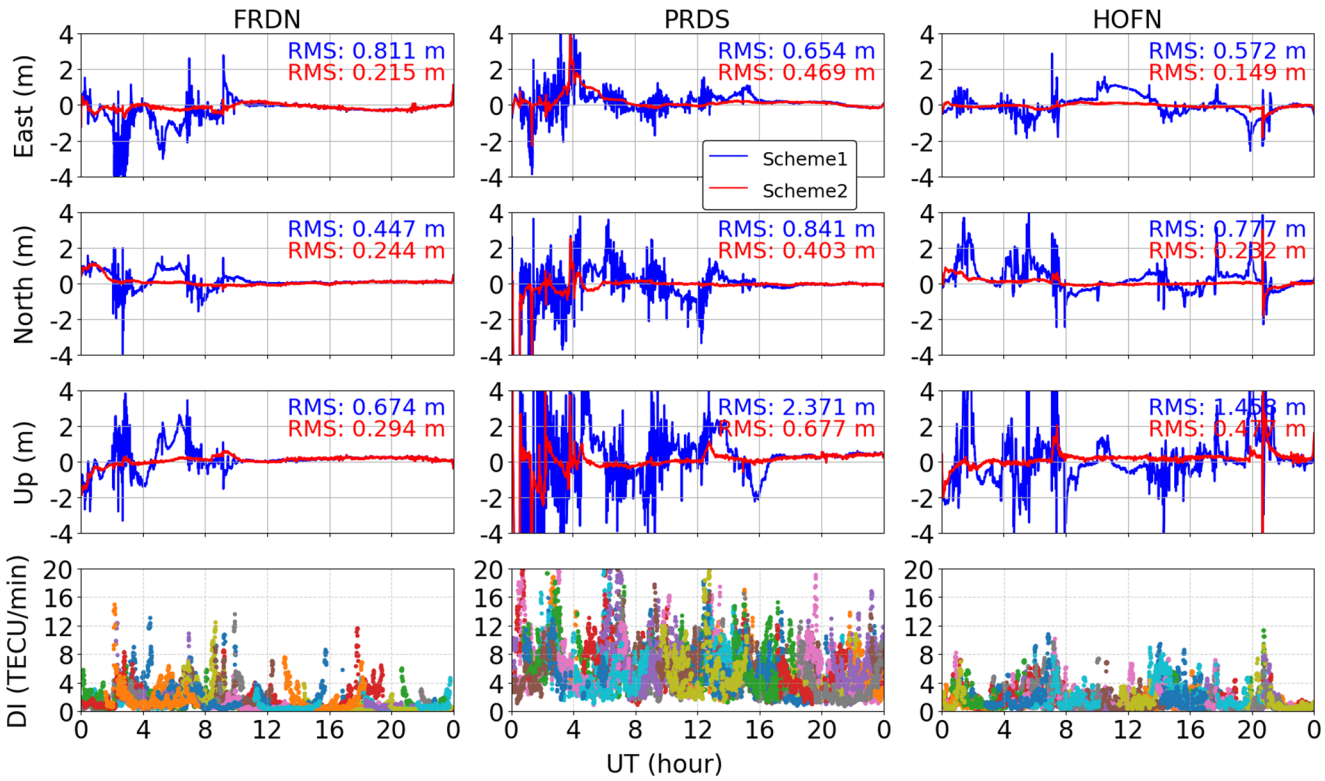


Fig. 5 Results comparison of kinematic PPP based on scheme1 (blue) and scheme2 (red) using GPS data from stations FRDN, PRDS, and HOFN on 11th May 2024

Table 2 Average root mean square values of kinematic PPP using schemes 1 and 2 in the horizontal and vertical components on 11th May 2024

	Scheme 1 (m)	Scheme 2 (m)	Improvement (%)
Horizontal	0.439	0.253	42.4
Vertical	0.759	0.477	37.2

2 screens out a large number of cycle slip misjudgments, thereby avoiding massive unnecessary ambiguity reinitialization, and as a result, greatly improving the positioning accuracy. Although the re-convergence of positioning still occurs in Scheme 2 during the extreme geomagnetic storm, for example, the reinitialization is still obvious at ~UT 21:00 of HOFN station, the positioning accuracy improvement is still obvious compared with Scheme 1.

The RMS values of kinematic PPP solution errors in the horizontal and vertical components of all 72 non-modeling stations on 11th May 2024 are calculated and summarized in Table 2. It can be easily concluded that the accuracy of Scheme 2 is significantly higher than that of Scheme 1, the proposed model outperforms the traditional fixed threshold with improvements of 42.4% and 37.2% in horizontal and vertical components, respectively.

Figure 6 shows the kinematic PPP results of 72 non-modeling stations using two schemes on the horizontal and vertical components on 11 May 2024. It can be noticed that on a global scale, scheme 2 has a significant improvement in positioning accuracy for both horizontal and vertical directions. The positioning errors of most stations are reduced, and the positioning accuracy is improved from decimeter-level to centimeter-level for some sites.

Kinematic PPP results during ionospheric disturbances on 11th October 2024

To validate the applicability of the proposed model in generalized ionospheric activities, data taken from 215 IGS stations on 11th October 2024 are processed and the results are analyzed, as there is also a large geomagnetic storm on that day. Similarly, Fig. 7 shows the PPP results of 3 IGS stations, FRDN (45.93° N, 66.66° W), PRDS (50.87° N, 114.29° W) and HOFN (64.27° N, 15.20° W). The convergence period of Scheme 1 suffers fluctuation because of false-detected cycle slips which lead to frequent ambiguity reset. By applying the adaptive cycle slip detection threshold model in Scheme 2, more tolerance is given in cycle slip detecting, which largely avoids the false detection and maintains high-accuracy positioning performance after convergence.

A loose GF threshold of 0.5 m is also applied for comparison and denoted as Scheme 3. Figure 8 shows the horizontal

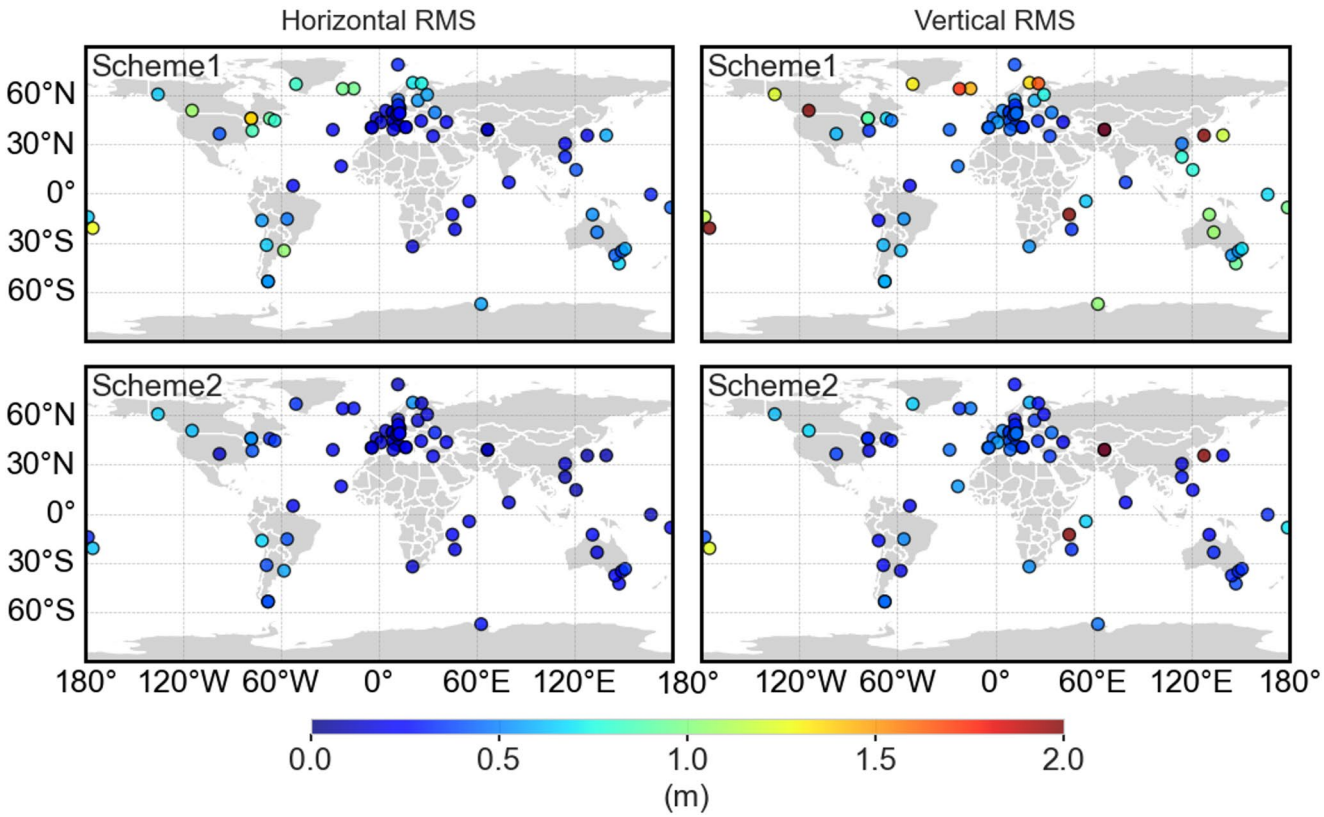


Fig. 6 Root mean square statistics of kinematic PPP with schemes 1 (upper) and 2 (bottom) in the horizontal and vertical components based on global positioning system data from 72 non-modeling International Global Navigation Satellite System Service stations on 11th May 2024

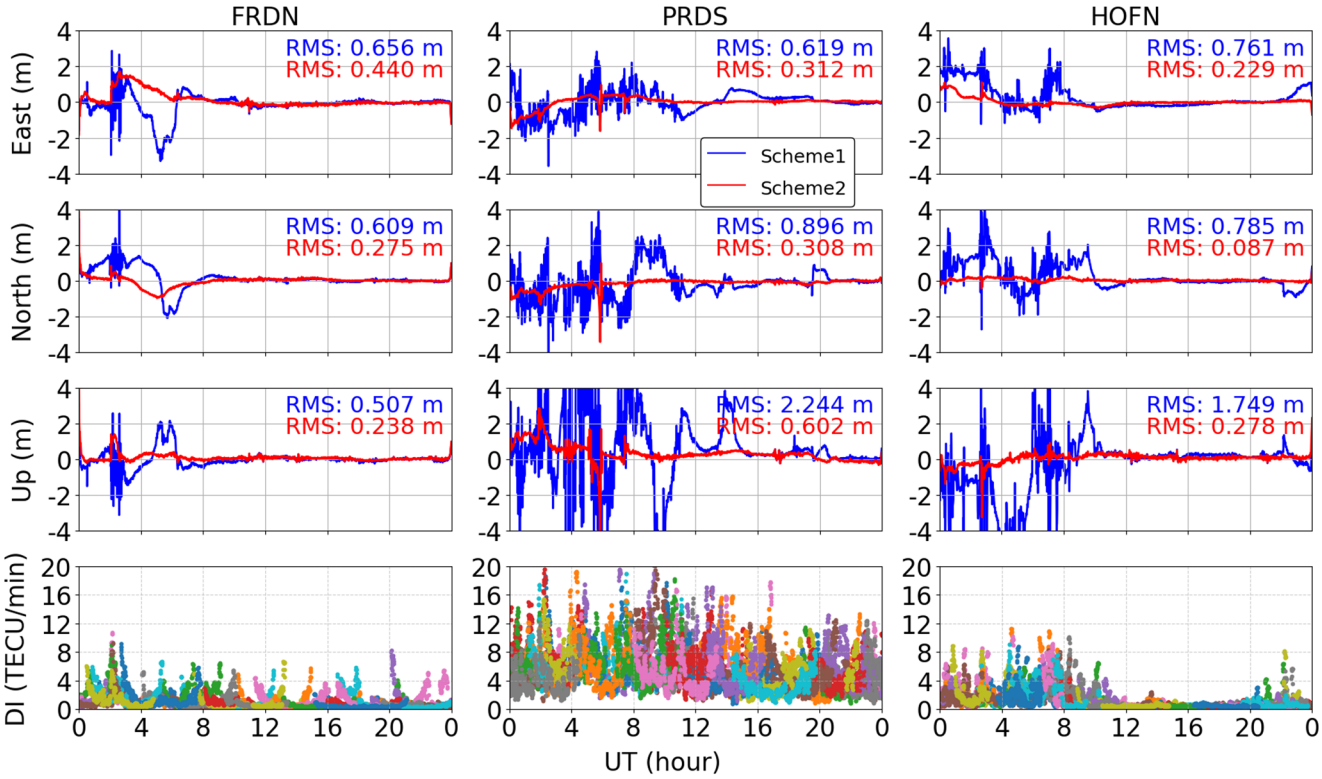


Fig. 7 Comparison results of kinematic precise point positioning based on scheme1 (blue) and scheme2 (red) using GPS data from stations FRDN, PRDS, and HOFN on 11th October 2024

and vertical RMS values of all experimental stations by the 3 schemes on 11th October 2024. Similar conclusion can be drawn that Scheme 2 outperforms Scheme 1, and the PPP accuracy of most stations is significantly improved in both horizontal and vertical components. Meanwhile, Scheme 3 also shows improvements compared to Scheme 1, which is as expected, as a loose threshold during ionospheric disturbances accommodate the irregular ionosphere change over time. Table 3 gives the average RMS statistics of the horizontal and vertical components from Schemes 1, 2 and 3, respectively, on 11th October 2024. Again, it is obvious that the horizontal and vertical accuracy is improved by 63.1% and 50.1% for Scheme 2 compared with Scheme 1. It is noteworthy that despite the average RMS of Scheme 3 is also better than Scheme 1, a fixed loose threshold is still worse than the proposed model. In conclusion, the proposed model not only has the best positioning performance among all schemes, but also has the ability of real-time response to different ionospheric periods.

Under the global-scale extreme ionospheric disturbance, there are still some ionospheric quiescence areas. If a loose fixed GF threshold is set only for global-scale ionospheric disturbances, it cannot adapt to different ionospheric behaviors in different areas. Figure 9 gives an example of this condition, for station MDVJ on the 11th October 2024 under slight ionospheric disturbance, significant spikes are noticed with Scheme 1 and 3 while the solutions seems to be stable for with the proposed model, and Scheme 2 performs better than Scheme 1 in terms of stability after convergence, showing good resistance to sudden ionospheric disturbances in a few epochs, which proves the reliability of adaptive threshold.

In addition, in order to analyze the performance of the model at different latitudes, we divide the stations into three categories by latitudes, with low latitudes ranging from 0 to 30 degrees, middle latitudes are from 30 to 60 degrees, and high latitudes are from 60 to 90 degrees. The results are summarized in Table 4. It can be seen that the average RMS of Scheme 2 is better than that of Schemes 1 and 3 in all latitude regions. Combined with the average DI of the stations in each latitude region given in Table 5, it can be found that the average daily DI in the high latitude region is higher than that in the middle and low latitude regions, indicating the adaptive model performs well in the strong ionospheric disturbance environment.

Kinematic PPP results during ionospheric quiescence on 9th July 2024

Lastly, data from 169 IGS stations on the ionospheric quiescence day of 9th July 2024 are processed to analyze the performance of the model in the ionospheric quiescence period.

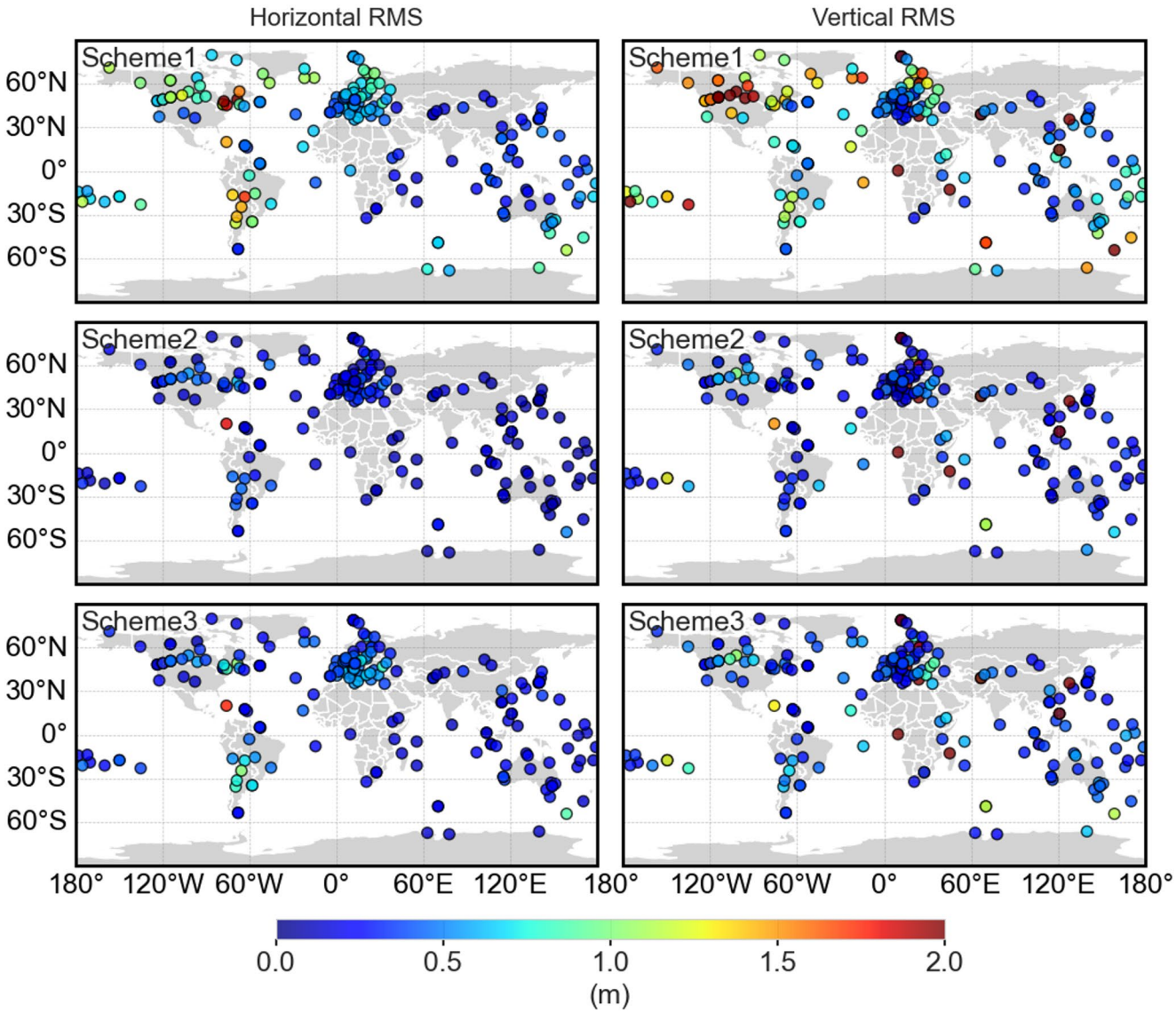


Fig. 8 Root mean square statistics of kinematic precise point positioning using schemes 1 (upper), 2 (middle) and 3 (bottom) in the horizontal and vertical components based on global positioning system data from 215 International Global Navigation Satellite System Service stations on 11th October 2024

Table 3 Average root mean square values of kinematic precise point positioning using schemes 1, 2 and 3 in the horizontal and vertical components on 11th October 2024

	Scheme 1 (m)	Scheme 2 (m)	Scheme 3 (m)	Improvement (%) (Scheme 2 vs. 1)
Horizontal	0.618	0.228	0.362	63.1
Vertical	0.867	0.433	0.522	50.1

Figure 10 shows the RMS of the three schemes in horizontal and vertical components on 9th July 2024. The positioning accuracy attenuation occurred in Scheme 3 in both components for some stations compared with Schemes 1 and 2, which means loose GF threshold failed to detect small cycle slips during ionospheric quiescence period. Table 6 shows the average RMS values of the 169 IGS stations in both horizontal and vertical components. In the horizontal component, Scheme 2 achieves improvements of 0.020 m and 0.009 m, respectively compared with Schemes 1 and 3, representing enhancements of 10.3% and 4.9%. In the vertical component, the accuracy is also improved by 0.015 m for Scheme 2 compared with Schemes 1 and 3. Adaptive GF threshold shows advantage over both fixed tight and loose threshold, effectively improving the positioning performance in ionospheric quiet period. Interestingly, Scheme 3 outperforms Scheme 1 in horizontal positioning accuracy for ~1 cm, as there could also be ionospheric bubbles even on ionospheric quiet days. Moreover, given that the IGS

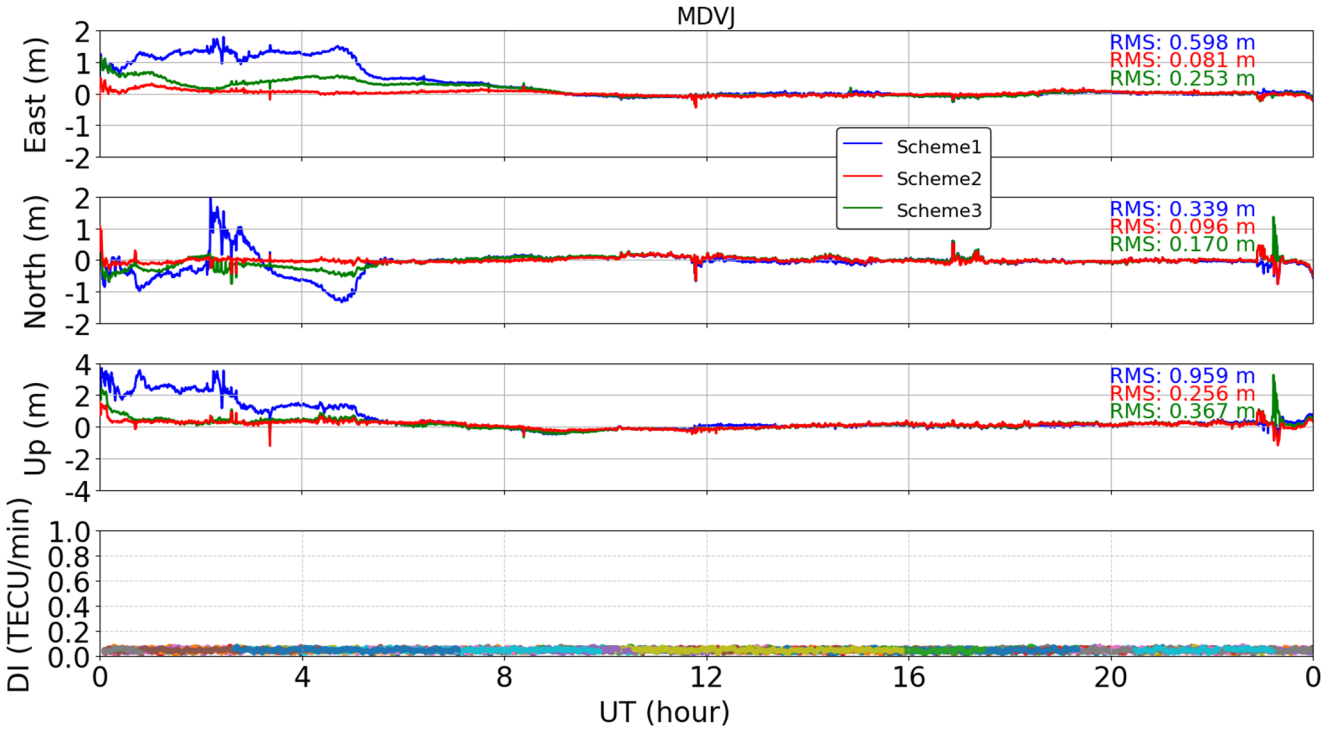


Fig. 9 Comparison results of kinematic precise point positioning based on scheme1 (blue), scheme 2 (red) and scheme3 (green) using GPS data from station MDVJ on 11th October 2024

Table 4 Average root mean square values of kinematic precise point positioning using schemes 1, 2 and 3 in the horizontal and vertical components at low, middle and high latitudes on 11th October 2024 (unit: m)

	Scheme 1			Scheme 2			Scheme 3		
Latitudes	Low	Middle	High	Low	Middle	High	Low	Middle	High
Horizontal	0.504	0.634	0.823	0.190	0.256	0.189	0.282	0.428	0.256
Vertical	0.855	0.768	1.351	0.509	0.368	0.544	0.583	0.482	0.554

Table 5 Average doppler index of low, middle and high latitude areas on 11th October 2024

Latitudes	Low	Middle	High
DI (TECU/min)	1.666	2.062	2.377

stations are selected, the observation conditions are relatively good, and the cycle slips are not that frequent, i.e., tight threshold is expected to be better when there are cycle slips, while thresholds have no impact on positioning errors when there are already no cycle slips.

Similarly, the average RMS of the three latitude regions are shown in Table 7. For the global ionospheric quiescence period on 9th July 2024, the positioning accuracy of Scheme 2 at three latitude regions is higher than Schemes 1 and 3, as the adaptive threshold of Scheme 2 effectively deals with the relatively gentle ionospheric changes. Combined with the average DI of the three latitude regions provided in Table 8, it can be concluded that in the low and high latitudes where the ionosphere is more active, Scheme 3 shows better performance than Scheme 1 due to the loose GF threshold. For the mid-latitude regions where the ionosphere is relatively stable, the loose threshold of Scheme 3 fails to effectively detect cycle slips, resulting in lower positioning accuracy than Scheme 1. The adaptive threshold of Scheme 2 effectively copes with the global ionospheric quiescence and regional ionospheric disturbances on the day, and has a positive effect on the positioning results of the three latitude regions.

Figure 11 shows another station-specific positioning time series instance. The station BAKE began to experience regional ionospheric disturbances from about 4:00 to 5:30 UT. The positioning accuracy of Schemes 1 and 3 in the East, North and Up directions is significantly affected during this period, showing frequent outliers and spikes in the time series of positioning errors. The positioning performance of Scheme 2 is only slightly affected, the RMSs of the three directions are obviously better than the other two schemes, which proves the applicability of the adaptive GF threshold model in the regional ionospheric disturbance environment.

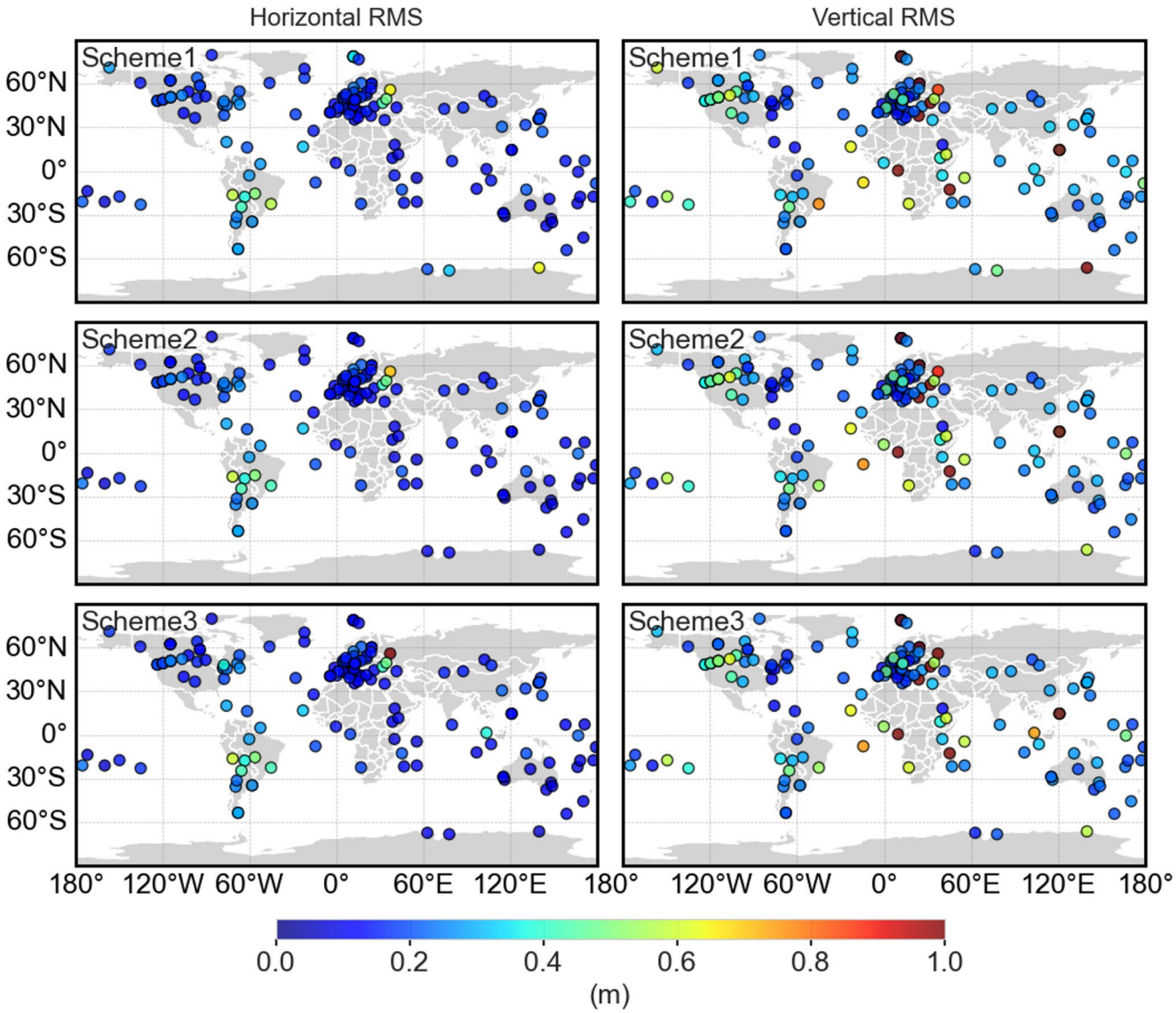


Fig. 10 Root mean square statistics of kinematic precise point positioning using schemes 1 (upper), 2 (middle) and 3 (bottom) in the horizontal and vertical components based on global positioning system data from 169 International Global Navigation Satellite System Service stations on 9th July 2024

Table 6 Average root mean square values of kinematic precise point positioning using schemes 1, 2 and 3 in the horizontal and vertical components on 9th July 2024 (unit: m)

	Scheme 1	Scheme 2	Scheme 3	Improvement (%) (Scheme 2 vs. 1)
Horizontal	0.194	0.174	0.183	10.3
Vertical	0.401	0.386	0.401	3.7

Table 8 Average doppler index of low, middle and high latitude areas on 9th July 2024

Latitudes	Low	Middle	High
DI (TECU/min)	1.851	1.760	1.963

Conclusions

GNSS measurements are easily affected by ionospheric

Table 7 Average root mean square values of kinematic precise point positioning using schemes 1, 2 and 3 in the horizontal and vertical components at low, middle and high latitudes on 9th July 2024

	Scheme 1 (m)			Scheme 2 (m)			Scheme 3 (m)		
Latitudes	Low	Middle	High	Low	Middle	High	Low	Middle	High
Horizontal	0.189	0.186	0.240	0.183	0.178	0.131	0.187	0.192	0.133
Vertical	0.496	0.302	0.661	0.486	0.301	0.575	0.494	0.322	0.575

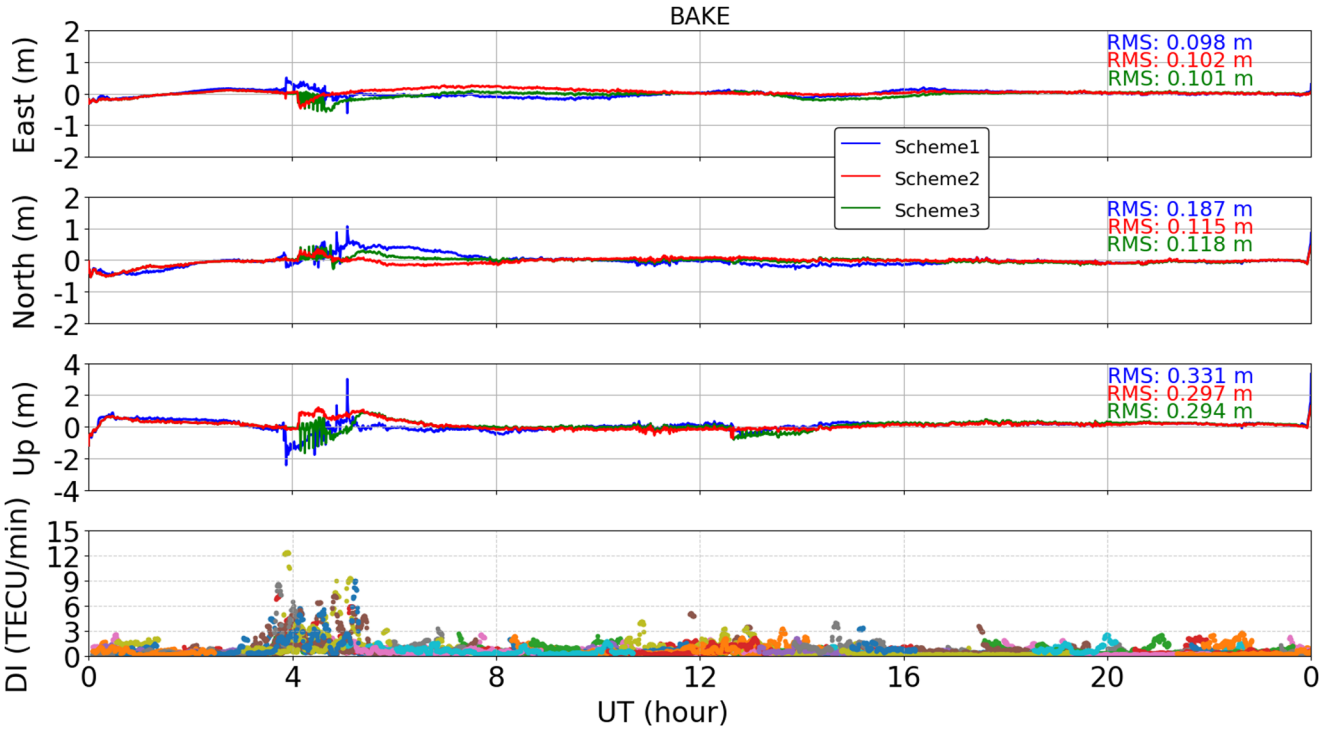


Fig. 11 Comparison results of kinematic precise point positioning based on scheme1 (blue), scheme 2 (red) and scheme3 (green) using GPS data from station BAKE on 9th July 2024

activities, therefore, a degraded positioning solution is usually obtained under complex ionospheric conditions. The fixed cycle slip detection threshold in traditional method will lead to frequent ambiguity reset. Moreover, the existing adaptive GF threshold model is based on ROTI, but the ROTI relies on TEC, and is already affected by cycle slips. Therefore, this study proposes to use DI, an index calculated from Doppler observations which is free from cycle slips, to establish an adaptive GF threshold model which effectively avoids the deficiency of ROTI.

In this study, the data of 110 IGS stations supporting Doppler data during the extreme geomagnetic storm on 11th May 2024 are used to establish the adaptive GF threshold model based on DI. The performance and effectiveness of the model is verified by using 72 and 215 IGS stations during the extreme geomagnetic storms on 11th May 2024 and 11th October 2024, respectively. Data of 169 IGS stations during another ionospheric quiescence period on 9th July 2024 are also used to verify the universality of the model. The GPS PPP results of 3 IGS stations with different latitudes show that the kinematic PPP accuracy with the proposed model is significantly improved compared to the conventional fixed GF threshold model, and the DI-based adaptive threshold avoids unnecessary ambiguity reset caused by false-detected cycle slips. The statistical results show that compared with the conventional fixed GF threshold model, the PPP solution accuracy of the DI-based adaptive GF threshold model is improved increased by 42.4% and 37.2% in the horizontal and vertical directions on 11th May 2024, respectively. Similarly, those improvements are 36.2% and 36.8% on 11th October 2024, showing significant mitigation of the impact of extreme geomagnetic storms on PPP. Moreover, the PPP results on 11th October 2024 and 9th July 2024 are analyzed in low, middle and high latitudes, respectively. The results show that for the global-scale ionospheric disturbance period, the adaptive model proposed in this study greatly improves the PPP accuracy in all latitude regions compared with tight threshold. The performance of the adaptive threshold model is also better than the loose threshold at all latitudes. For the global-scale ionospheric quiescence period, the adaptive model improves PPP accuracy in both horizontal and vertical components compared with tight and loose thresholds, especially during small-scale regional ionospheric disturbances.

With results from different days, the proposed method shows superior positioning performance, demonstrating the correctness, efficiency, and uniformity. In conclusion, the proposed DI-based adaptive cycle slip detection threshold has the potential to be widely applied in location-based-service applications, aiming to provide robust and continuous high-accuracy GNSS solutions.

Acknowledgements The authors acknowledge the CDDIS for providing the GNSS data.

Author contributions L.T. and L.Z. wrote the main manuscript text and prepared Figs. 4, 5, 6, 7, 8, 9, 10 and 11 and F.X. prepared Figs. 1, 2 and 3 and data, X.Z. modified the manuscript and J.H. supervised the research and modified the manuscript. All authors reviewed the manuscript.

Funding Open access funding provided by The Hong Kong Polytechnic University. This study was funded by the National Natural Science Foundation of China (Grant No. 42274017), Guangdong Basic and Applied Basic Research Foundation (Grant No. 2023A1515030184) and Guangzhou Science and Technology Plan Project (Grant No. 2025A04J5190).

Data availability GPS data are available from the website at https://cddis.nasa.gov/archive/gnss/data/daily/.

Declarations

Consent for publication The authors have read and understood the publishing policy and agree to submit and publish this manuscript in accordance with this policy.

Competing interests The authors declare no competing interests.

Ethical approval and consent to participate The authors declare compliance with the ethics standard required by GPS Solutions. This study has no potential conflicts of interest and does not involve human participants and animals.

Open Access This article is licensed under a Creative Commons Attribution 4.0 International License, which permits use, sharing, adaptation, distribution and reproduction in any medium or format, as long as you give appropriate credit to the original author(s) and the source, provide a link to the Creative Commons licence, and indicate if changes were made. The images or other third party material in this article are included in the article's Creative Commons licence, unless indicated otherwise in a credit line to the material. If material is not included in the article's Creative Commons licence and your intended use is not permitted by statutory regulation or exceeds the permitted use, you will need to obtain permission directly from the copyright holder. To view a copy of this licence, visit http://creativecommons.org/licenses/by/4.0/.

References

Banville S, Langley RB (2012) Cycle-slip correction for single frequency PPP. In: Proceedings of the ION GNSS 2012. Institute of Navigation, Nashville, Tennessee, USA, September 17–21, pp3053–3061

Chen W, Gao S, Hu C, Chen Y, Ding X (2008) Effects of ionospheric disturbances on GPS observation in low latitude area. GPS Solut 12(1):33–41. https://doi.org/10.1007/s10291-007-0062-z

Danilchuk E, Yasyukevich Y, Vesnin A, Klyusilov A, Zhang B (2025) Impact of the May 2024 extreme geomagnetic storm on the ionosphere and GNSS positioning. Remote Sens 17(9):1492. https://doi.org/10.3390/rs17091492

Junbo Shi C, Xu J, Guo Y Gao (2015) Real-Time GPS precise point Positioning-Based precipitable water vapor Estimation for rainfall monitoring and forecasting. IEEE Trans Geosci Remote Sens 53(6):3452–3459. https://doi.org/10.1109/TGRS.2014.2377041

Kouba J, Héroux P (2001) Precise point positioning using IGS orbit and clock products. GPS Solut 5(2):12–28. https://doi.org/10.1007/PL00012883

Li X, Ge M, Zhang X, Zhang Y, Guo B, Wang R, Klotz J, Wickert J (2013) Real-time high-rate co-seismic displacement from ambiguity-fixed precise point positioning: application to earthquake early warning. Geophys Res Lett 40(2):295–300. https://doi.org/10.1002/grl.50138

Liu T, Zhang B, Yuan Y, Li Z, Wang N (2019) Multi-GNSS triple-frequency differential code bias (DCB) determination with precise point positioning (PPP). J Geod 93(5):765–784. https://doi.org/10.1007/s00190-018-1194-3

Lu Y, Wang Z, Ji S, Chen W (2020) Assessing the positioning performance under the effects of strong ionospheric anomalies with Multi-GNSS in Hong Kong. Radio Sci 55(8):e2019RS007004. https://doi.org/10.1029/2019RS007004.

Luo X, Gu S, Lou Y, Xiong C, Chen B, Jin X (2018) Assessing the performance of GPS precise point positioning under different geomagnetic storm conditions during solar cycle 24. Sensors 18(6):1784. https://doi.org/10.3390/s18061784

Luo X, Du J, Galera Monico JF, Xiong C, Liu J, Liang X (2022) ROTI-Based stochastic model to improve GNSS precise point positioning under severe geomagnetic storm activity. Space Weather 20(7):e2022SW003114. https://doi.org/10.1029/2022SW003114

Luo X, Xie Z, Monico JFG, Zhang B, Pereira VAS, Lou Y (2023) An ionospheric scintillation index derived from dual-frequency doppler measurements released by geodetic GNSS receivers operating at 1 hz. J Geod 97(7):70. https://doi.org/10.1007/s00190-023-01760-y

Marques HA, Marques HAS, Aquino M, Veettil SV, Monico JFG (2018) Accuracy assessment of precise point positioning with multi-constellation GNSS data under ionospheric scintillation effects. J Space Weather Space Clim 8:A15. https://doi.org/10.1051/swsc/2017043

Moreno B, Radicella S, De Lacy MC, Herraiz M, Rodriguez-Caderot G (2011) On the effects of the ionospheric disturbances on precise point positioning at Equatorial latitudes. GPS Solut 15(4):381–390. https://doi.org/10.1007/s10291-010-0197-1

Rodríguez-Bilbao I, Radicella SM, Rodríguez-Caderot G, Herraiz M (2015) Precise point positioning performance in the presence of the 28 October 2003 sudden increase in total electron content. Space Weather 13(10):698–708. https://doi.org/10.1002/2015SW001201

Yang Z, Morton YTJ, Zakharenkova I, Cherniak I, Song S, Li W (2020) Global view of ionospheric disturbance impacts on kinematic GPS positioning solutions during the 2015 St. Patrick's day storm. J Geophys Res Space Phys 125(7):e2019JA027681. https://doi.org/10.1029/2019JA027681

Zakharenkova I, Cherniak I (2021) Effects of storm-induced Equatorial plasma bubbles on GPS-based kinematic positioning at Equatorial and middle latitudes during the September 7–8, 2017, geomagnetic storm. GPS Solut 25(4):132. https://doi.org/10.1007/s10291-021-01166-3

Zhang X, Andersen OB (2006) Surface ice flow velocity and tide retrieval of the Amery ice shelf using precise point positioning. J Geod 80(4):171–176. https://doi.org/10.1007/s00190-006-0062-8

Zhang X, Guo F, Zhou P (2014) Improved precise point positioning in the presence of ionospheric scintillation. GPS Solut 18(1):51–60. https://doi.org/10.1007/s10291-012-0309-1

Zhang F, Chen W, Xu F, Zou F, Deng Y, Tang L (2025) Equatorial plasma bubble detection based on GNSS doppler index using support vector machine algorithm. GPS Solut 29(2):60. https://doi.org/10.1007/s10291-025-01820-0

Zumberge JF, Heflin MB, Jefferson DC, Watkins MM, Webb FH (1997) Precise point positioning for the efficient and robust

analysis of GPS data from large networks. J Geophys Res Solid Earth 102(B3):5005–5017. https://doi.org/10.1029/96JB03860

Publisher's note Springer Nature remains neutral with regard to jurisdictional claims in published maps and institutional affiliations.



Long Tang is an Associate Professor at the Guangdong University of Technology, China. He received a Ph.D. in geodesy and surveying engineering from Wuhan University in 2015. His current research interests include GNSS precise positioning and ionospheric monitoring.



Luheng Zhou is currently a master's degree candidate at Guangdong University of Technology, China. His current research focuses, mainly involve GNSS precise positioning.



Fan Xu is currently a master's degree candidate at Guangdong University of Technology, China. His current research focuses, mainly involve GNSS ionospheric monitoring.



Jiahuan Hu is a postdoctoral fellow at The Hong Kong Polytechnic University. He received his Ph.D. at York University, Canada, in 2024, and M.Sc. degree at Wuhan University, China, in 2020. His main research interests are GNSS ambiguity resolution, PPP-RTK, and smartphone precise positioning.



Xiaohong Zhang is a Professor at the Wuhan University, China. He received a Ph.D. in geodesy and surveying engineering from Wuhan University in 2002. His main research interests include precise point positioning and GNSS applications.